Chemical Science

ROYAL SOCIETY OF CHEMISTRY

EDGE ARTICLE

View Article Online
View Journal | View Issue

Cite this: *Chem. Sci.*, 2025, **16**, 10842

All publication charges for this article have been paid for by the Royal Society of Chemistry

Received 6th March 2025
Accepted 4th May 2025

DOI: 10.1039/d5sc01799h

rsc.li/chemical-science

Multi-site orbital coupling in Ru-based high-entropy alloy-enabled hydroxyl spillover for enhanced peroxidase-like activity†

Qi Yang,‡[ab] Jiawei Zhang,‡[a] Yuxi Tang,[a] Yan Ju,[a] Xuejiao Gao, *[c] Chaoyang Chu,[d] Huimin Jia *[ab] and Weiwei He *[ab]

Peroxidase (POD)-like nanozymes are attracting increasing attention in anti-tumor, antibacterial, disease diagnosis, and environmental applications. However, simultaneously improving the POD-like activity and stability of nanozymes remains a non-trivial challenge. Inspired by the excellent stability and multiple active sites of high-entropy alloys, we design a Ru-based (RuPtIrRhCu) high-entropy alloy nanozyme (HEAzyme) with improved catalytic activity and stability. Benefiting from the strong adsorption capacity of Ru toward hydrogen peroxide (H_2O_2)/hydroxyl (OH) and the collaborative effect induced by the multiple elements, an interesting "hydroxyl spillover" route is triggered on the RuPtIrRhCu HEAzymes. The efficient dissociated adsorption of H_2O_2 and fast transfer of adsorbed hydroxyl (*OH, * denotes the adsorbed state) is achieved, resulting in boosted POD-like activity. The POD-like activity of the HEAzyme remained unchanged for 6 months, exhibiting outstanding stability. A multi-channel colorimetric sensor array was developed to specifically identify eight biological antioxidants, especially for the chiral recognition of L-cysteine (L-Cys) and D-cysteine (D-Cys). This study not only provides an effective, multi-site collaborative mechanism for improving POD-like activity and stability but also extends the horizons and perspectives in nanozymes.

Introduction

Nanozymes are nanoscale biocatalysts with enzyme-like catalytic activity, which offer advantages, such as high stability, low cost, and easy modification over natural enzymes and show great promise in wide applications.[1–8] Since the accidental discovery of the peroxidase (POD)-like activity of Fe_3O_4 nanoparticles (NPs), a great deal of nanozymes with POD-like activity have been emerged and used in biosensing, environmental monitoring, disease diagnosis, and treatments.[9,10] Currently, continuous improvement of POD-like activity and stability of nanozymes has become a key issue to facilitate their practical applications.[11–14] The POD-like ability is determined by the H_2O_2 decomposition mechanism on nanozyme surface, which has been described as: $H_2O_2^* \rightarrow 2HO^* \rightarrow H_2O^* + O^*$.[15] The dissociated adsorption of H_2O_2 (producing substantial *OH) and desorption of *OH plays a critical role in the catalytic reaction. However, an inherent contradiction exists between *OH adsorption and desorption for a certain active site on the catalytic interface of metallic nanozymes.[16–18] Specifically, excessively weak adsorption affinity will cause insufficient *OH to participate in the subsequent reaction, while excessively strong adsorption affinity may result in blockage of numerous *OH and retardation of the subsequent desorption and oxidation. This suggests optimal catalytic activity is derived from metallic nanozymes with moderate adsorption affinity.[19] Obviously, this "compromise strategy" still has scope for improvement because it does not maximize the performance of adsorption and desorption of nanozymes but only reconcile the competition between them. Exploring novel catalytic mechanisms and pathways is urgent and necessary, if we want to further enhance the POD-like activity of metallic nanozymes.

Inspired by the "hydrogen spillover" (H* spillover) mechanism in electrocatalysis field, we assume that for nanomaterials, especially multi-component alloys with abundant and complex active sites, the active sites with strong adsorption can capture H*, while active sites with weak adsorption favor

[a]*Key Laboratory of Micro–Nano Materials for Energy Storage and Conversion of Henan Province, Institute of Surface Micro and Nano Materials, College of Chemical and Materials Engineering, Xuchang University, Xuchang, Henan 461000, P. R. China. E-mail: jhmxcu2015@163.com; heweiweixcu@gmail.com*

[b]*Henan Joint International Research Laboratory of Nanomaterials for Energy and Catalysis, Xuchang University, Xuchang, Henan 461000, China*

[c]*College of Chemistry and Chemical Engineering, Jiangxi Normal University, Nanchang 330022, P. R. China. E-mail: gaoxj@jxnu.edu.cn*

[d]*Shanghai Key Laboratory of High-resolution Electron Microscopy, School of Physical Science and Technology, ShanghaiTech University, China*

† Electronic supplementary information (ESI) available: Additional experimental section details, Tables S1–S3 and Fig. S1–S6 (PDF). See DOI: https://doi.org/10.1039/d5sc01799h

‡ These authors contributed equally to this work and should be considered co-first authors.

resultant desorption and product formation. Studies have shown that H* could migrate between adsorption and desorption sites to maximize the functions of different components, greatly accelerating the catalytic process and improving catalytic efficiency.[20–22] It is reasonable to infer that a similar mechanism could be applied to the catalytic process in which hydroxyl groups serve as intermediates. Recently, two hybrid nanomaterials ($Cr_{0.2}Ru_{0.8}O_{2-x}$ and Ru–Sn/SnO_2) have been reported to introduce outstanding hydroxyl (*OH) spillover effect in oxygen evolution reaction (OER) and hydrogen evolution reaction (HER), respectively.[23,24] The researchers proposed that excellent adsorption affinity of Ru element to *OH is the key to achieving the hydroxyl spillover effect. Coincidentally, in our previous studies, nanoalloy with Ru element was verified to possess excellent POD-like activity.[14,25] We assume that in Ru-based alloys, the *OH could authentically transfer from Ru to other active sites, avoiding the local accumulation and blockage of *OH on Ru active sites, facilitating the subsequent desorption and oxidation and thus greatly improving the POD-like performance. In this regard, designing Ru-based multimetallic nanozymes, optimizing hydroxyl adsorption, and accelerating *OH transfer present a potential opportunity to overcome the limitations of POD-like activity. However, the catalytic activity of multimetallic nanozymes might be largely limited by their atomic migration, which results in polyphase alloys.[26–28] Therefore, it is necessary to achieve a combination of high catalytic activity and stability.

High-entropy alloys (HEAs) is commonly defined as alloys containing at least 5 different elements with 5–35% atom percent of each component. That means, the principal elements are mixed in near-equal atomic ratios and no particular element dominates. The formation enthalpy of HEAs is overcome by the dramatic increment of configurational entropy induced, facilitating the formation of stable single-phase solid solutions rather than intermetallic compounds.[29,30] Therefore, HEAs break the immiscible gap of elements and supplies numerous possible atomic arrangements on the surface.[31,32] That means, HEAs can provide a unique surface and electronic structure compared to conventional alloys. On the one hand, the high entropy effect and hysteresis diffusion effect bring excellent phase stability to HEAs structures.[26,27,33] On the other hand, fine-tuning the principal elements of HEAs could adjust the electronic and geometric configurations to a large extent, which helps to achieve optimized catalytic performance through inherent synergy.[28,34,35] More critically, abundant active sites on the surface of HEAs provide more space for the compatibility design of *OH adsorption energy ($E_{abs,\ OH}$),[36–38] which is conducive to constructing a suitable adsorption energy gradient to achieve strong adsorption and fast transfer of *OH. Therefore, introducing the proposed Ru-based multimetallic active sites into HEAs seems to provide an effective countermeasure for developing novel nanozymes with highly boosted POD-like performance.

Here, we rationally designed and successfully synthesized a Ru-based RuPtIrRhCu HEA nanozyme (HEAzyme). Four compatible assistants (Pt, Ir Rh and Cu) were selected to serve as the competitive adsorption sites for Ru. We hope the RuPtIrRhCu HEAzymes obtain element matching-mediated hydroxyl spillover mechanism, by which *OH adsorbed on Ru scan be transferred to the adjacent Pt, Ir, Rh, or Cu active sites to generate H_2O* and be desorbed, improving the catalytic kinetics. Density functional theory (DFT) analysis confirmed that the orbital coupling of five components modulate the d-band center of HEAzymes to an appropriate position and the hydroxyl spillover from Ru to other active sites is energetically favorable. The prepared RuPtIrRhCu HEAzymes was endowed superior peroxidase POD-like activity and stability compared to that of natural horseradish peroxidase (HRP) and five kinds (Pt, Ir, Ru, Rh, Cu) of single metal NPs. Using the superior POD-like activity of RuPtIrRhCu HEAzymes, a multi-channel colorimetric sensing platform was developed for identification of various antioxidants, especially for chiral discrimination of L-cysteine and D-cysteine. Our work reveals that Ru-based multi-element matching, which facilitates hydroxyl spillover, represents a promising strategy for designing nanoenzymes that mimic PODs.

Experimental section

Chemicals and materials

The chemicals purchased from Sinopharm are as follows: potassium chloroplatinite(II) (K_2PtCl_4), potassium chlororhodiate (K_2RhCl_6), ruthenium chloride ($RuCl_3$), iridium chloride ($IrCl_3$), copper chloride dihydrate ($CuCl_2 \cdot 2H_2O$), polyvinyl pyrrolidone (PVP K30), ascorbic acid (AA), hydrogen peroxide (H_2O_2), 3,3′,5,5′-tetramethylbenzidine (TMB), 5,5-dimethylpyrroline *N*-oxide (DMPO), ethylene glycol (EG), acetone, L-cysteine (L-Cys), D-cysteine (D-Cys), reduced glutathione (GSH), acetylcysteine (NAC), sodium bisulfide (NaSH), tannic acid (TA), gallic acid (GA), dopamine (DA), L-histidine (L-His), L-glutamic acid (L-Glu), L-lysine (L-Lys), L-tyrosine (L-Tyr), L-tryptophan (L-Try), L-leucine (L-Leu), aspartate (L-Asp). All experimental preparations were washed with ultra-pure water (18 MΩ cm) and aqua regia solution (HNO_3/HCl = 1 : 3 v/v).

Characterization

The transmission electron microscopy (TEM) images were captured on a Tecnai G2 F20 U-TWIN electron microscope with an accelerating voltage of 200 kV. This microscope was also used to obtain high-resolution TEM (HRTEM) images, selected area electron diffraction (SAED) patterns and high angle angular dark field-scanning transmission electron microscopy-energy dispersive X-ray spectrometer (HAADF-STEM-EDS). The crystal structure of the samples was detected by X-ray diffraction (XRD, Bruker D8-Advance), with Cu-Kα radiation ($\lambda = 1.5406$ Å). The absorption curves were measured by a UV-vis-NIR spectrophotometer (Varian Cary 5000). The elemental ratios were determined applying an Agilent 7800 inductively coupled plasma-mass spectrometry (ICP-MS). The X-ray photoelectron spectroscopy (XPS) was conducted using a Thermo ESCALAB 250XI multifunctional imaging electron spectrometer using 150W Al Kα radiation and a base pressure of approximately 3×10^{-9} mbar. The binding energies were calibrated to the C 1s line

at 284.8 eV. The electron spin resonance (ESR) spectroscopy were recorded using an EMX micro electron paramagnetic resonance spectrometer (Bruker EMXmicro). The measurements were carried out at room temperature under the following conditions: microwave power 2 mW, modulation amplitude 1.0 G, attenuation 20 dB, and scan range of 100 G.

Synthesis of RuPtIrRhCu HEAzymes

RuPtIrRhCu HEAzymes were prepared by one-pot co-reduction of multiple metal ions in EG solution. Typically, a desirable volume of 20 mM K_2PtCl_4, K_2RhCl_6, $RuCl_3$, $IrCl_3$ and $CuCl_2$, according to Pt/Ir/Ru/Rh/Cu feeding molar ratio of 1 : 1 : 1 : 1 : 1, were first added to EG solution containing 220 mg PVP and evenly mixed. Then 2.5 mL AA solution with a concentration of 80 mM was added to the mixture and transferred to the reactor, where it was reacted at 200 °C for 6 h and cooled to room temperature. 30 mL acetone was added to the cooled solution and centrifuged at 10 000 rpm for 15 min to obtain the precipitated product. Finally, HEAzymes solution with a concentration of 10 mM was obtained by adding deionized water to the precipitated product at a constant volume of 4 mL. The corresponding pure metal Pt, Ir, Ru, Rh, Cu NPs were prepared by the same procedure to that of HEAzymes, except that only one metal precursor with fixed concentration was added into the reaction vessel.

Assays for peroxidase- and oxidase-like activity of RuPtIrRhCu HEAzymes

The POD- and Oxidase (OXD)-like activity of RuPtIrRhCu HEAzymes and single metal NPs were studied by catalytic oxidation of TMB with or without hydrogen peroxide (H_2O_2) at 25 °C. First, we mixed 20 μL 20 mM TMB with 20 μL 0.1 M H_2O_2 in 3 mL H_2O. Then, 5 μL 1 mM RuPtIrRhCu HEAzymes suspension was added to initiate the oxidation of TMB. The oxidation of TMB and its accompanying color change were monitored and measured by UV-vis absorption spectrometry. The kinetics of catalytic oxidation of TMB was evaluated using scanning kinetic model and recording absorption spectra every 1 min. The apparent kinetic parameters were calculated at 25 °C based on the Michaelis–Menten equation (eqn (1) and (2)),

$$v = \frac{V_{max}[S]}{K_m + [S]} + \frac{1}{[S]} \quad (1)$$

$$\frac{1}{v} = \frac{K_m}{V_{max}[S]} + \frac{1}{V_{max}} \quad (2)$$

where v is the reaction initial velocity, V_{max} is the maximal reaction velocity, $[S]$ is the concentration of substrate, and K_m is the Michaelis-constant. The ability of single metal and RuPtIrRhCu HEAzymes to generate hydroxyl radical (˙OH) during the catalytic process was evaluated through ESR technique. The solution containing 10 μL of 100 mM H_2O_2 and 5 μL 250 mM DMPO is set as the blank control. 5 μL 0.4 mM Ru, Pt, Ir, Rh, Cu, or RuPtIrRhCu HEAzymes was added to the control solution, respectively. The characteristic peak of DMPO/˙OH was monitored during 0–3 min. Furthermore, the adsorption capacity of single metal and RuPtIrRhCu HEAzymes to ˙OH was also evaluated. The H_2O_2/Fe^{2+} system (10 μL of 100 mM H_2O_2 and 10 μL of 10 mM Fe^{2+}) was used to produce ˙OH and DMPO (5 μL, 250 mM) was also chosen as the spin label. Then 5 μL 0.4 mM Ru, Pt, Ir, Rh, Cu, or RuPtIrRhCu HEAzymes was added. The characteristic peak of DMPO/˙OH was monitored during 0–3 min.

Multi-channel colorimetric sensor array for discriminating antioxidants

The significantly enhanced peroxidase-like ability of RuPtIrRhCu HEAzymes were applied for biosensing of different antioxidants. The mixture of 100 μL 0.1 mM RuPtIrRhCu HEAzymes solution, 2.7 mL sodium phosphate dibasic-citric acid buffer (pH = 3), 20 μL 20 mM TMB, and 20 μL 0.1 M H_2O_2 were used to construct a TMB multi-channel color reaction system, which catalyzed by the HEAzymes. In the identification of different antioxidants, we pre-mixed 100 μL 0.1 mM HEAzymes with 200 μL 0.2 mM different antioxidants (L-Cys, D-Cys, GSH, NaSH, NAC, TA, GA, DA). It was incubated at room temperature at 25 °C for 10 min, and then the absorption spectrum was measured using UV-vis absorption spectrometer. The experiment was repeated five times. Finally, principal component analysis of eight kinds of antioxidants was performed by Origin lab 2019.

Detection of L-cysteine and real sample containing acetylcysteine

For L-Cys colorimetric detection, 100 μL HEAzymes and 200 μL L-Cys with different concentrations (1, 5, 10, 20, 40, 60, 80, 100, 120, 140 μM) were incubated at 25 °C for 10 min. Then 2.7 mL pH = 3 buffer solution, 20 μL of 20 mM TMB, and 20 μL of 0.1 M H_2O_2 were added in sequence. The mixture was reacted at room temperature of 25 °C for 30 min, and then the UV-vis spectrum was measured. Each test was repeated five times. The absorption intensity at 370 nm, 450 nm, and 650 nm was recorded for quantification. Compared with 200 μL 100 μM L-Cys, 200 μL 4 mM L-Glu, L-Lys, L-Tyr, L-Trp, L-Leu, L-Asp, and L-His were used as interferents, respectively, to evaluate the selectivity in L-Cys detection. The standard addition method was used to test the NAC concentration in a clinical complex amino acid injection. First, 100 μL of HEAzymes and 200 μL of complex amino acid injection with diluted concentrations (ranging from 0.05 to 0.2 mM) were added separately into centrifuge tubes. Second, NAC standard solutions with different concentrations were added into the mixed solution, respectively, and incubated at room temperature for 10 min. After repeating the operations described in Section 2.4 and 2.6, the absorbance at 650 nm was tested by UV-vis. Then the equation of absorbance to standard solution concentration was fitted and the NAC concentration in the real sample could be obtained. Each concentration of amino acid injection was tested three times.

Results and discussion

The information of DFT calculations is provided in the ESI.†

Formation of RuPtIrRhCu high-entropy alloy nanozymes

Fig. 1a describes the synthesis of RuPtIrRhCu HEAzymes through hydrothermal treatment of the mixed metal ions in the presence of PVP and AA. This facile and environmentally friendly method affords HEA NPs with small particle size and good water dispersion, and has universal applicability for synthesizing noble metal-based HEA NPs. The XRD pattern displayed only one significant diffraction peak at 40.2° for (111) facets (Fig. 1b and S1†). The simple characteristic peak indicates that RuPtIrRhCu HEAzymes were formed as a solid solution with face-centred cubic (FCC) alloy structure, rather than a complex intermetallic compound. The broadening of peaks and the reduction in intensity in the XRD pattern are attributed to the small particle size and significant lattice distortion of the RuPtIrRhCu HEAzymes. The HRTEM images reveal an average lattice spacing of 0.220 nm for RuPtIrRhCu HEAzymes (Fig. 1c), between the lattice spacing values of (111) facets in Pt (0.227 nm), Ir (0.221 nm), Ru (0.213 nm), Rh (0.220 nm), and Cu (0.208 nm), further confirming an FCC crystal phase of RuPtIrRhCu HEAzymes. Notably, Fourier transform analysis (FFT) revealed the lattice spacing values of 0.216 (Zone 1), 0.221 (Zone 2) and 0.224 nm (Zone 3) (Fig. 1f), demonstrating lattice distortions in the synthesized HEAzymes, as shown in Fig. 1c. In addition, crystal defects, such as dislocations (marked by white T-lines), vacancies (marked by white dashed circle) and grain boundaries (marked by white dashed cross lines) observed in HEAs are also shown in Fig. 1c. The SAED results shown in Fig. 1d also illustrated a typical FCC phase, which is consistent with previous XRD and HRTEM results. The elemental mapping from HAADF-STEM-EDS revealed the distribution of Pt, Ir, Rh, Ru, and Cu in the RuPtIrRhCu HEAzymes, verifying the successful preparation of quinary alloy (Fig. 1e). The ICP-MS characterization in Fig. 1g showed that the corresponding atomic ratios of Ru, Pt, Ir, Rh, and Cu were 22.74 : 26.30 : 12.83 : 12 : 08 : 26.05, with a conformational entropy of 1.56 R (molar gas constant), which belongs to the high entropy category (≥1.5 R). The average

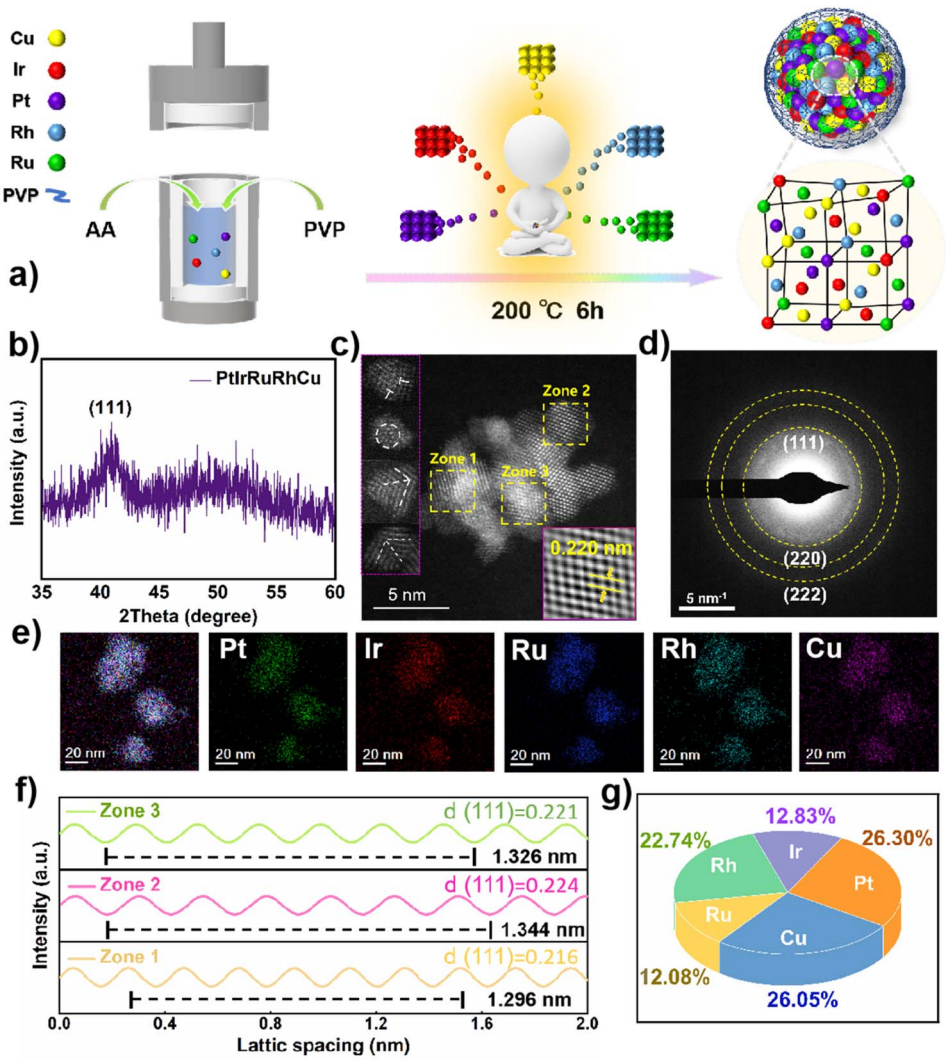

Fig. 1 Preparation and characterization of the RuPtIrRhCu HEAzymes. (a) Schematic diagram of the synthesis process of the RuPtIrRhCu HEAzymes. (b) XRD pattern. (c) HRTEM images, with the inset diagram for the representative atomic arrangement. (d) SAED pattern. (e) HAADF-STEM-EDS mapping characterization. (f) Integrated pixel intensity of RuPtIrRhCu HEAzymes from zone 1–3 in (c). (g) Elemental ratios from ICP-MS.

diameter was analyzed based on 100 randomly chosen particles, and the result was calculated to be 3.63 ± 0.40 nm (Fig. S2†). The XPS characterization (Fig. S3†) further confirmed the introduction of five metallic elements (Ru, Pt, Ir, Rh, and Cu in Fig. S3a†) and detailed the valence data of them (Fig. S3b–f†). The binding energies at 484.4 and 462.0 eV are attributed to $3p_{1/2}$ and $3p_{3/2}$ of Ru^0, respectively (Fig. S3b†). The peaks at 71.1 and 71.8 eV are attributed to $4f_{7/2}$ of Pt^0 and Pt^{2+}, respectively (Fig. S3c†). The peaks at 60.8 and 61.4 eV are assigned to $4f_{7/2}$ of Ir^0 and Ir^{3+}, respectively (Fig. S3d†). The peaks at 307.1 and 309.7 eV correspond to $3d_{5/2}$ of Rh^0 and Rh^{3+}, respectively (Fig. S3e†). For Cu 2p, Cu^0 $2p_{3/2}$ and Cu^{2+} $2p_{3/2}$ are concentrated at 931.9 and 933.3 eV, respectively (Fig. S3f†). Notably, Pt, Ir, Rh, and Cu elements in RuPtIrRhCu HEAzymes displayed mixed metallic and oxidized valence states, while the Ru element was presented only in the metallic state. This could positively influence *OH adsorption and charge transfer at Ru sites.

Superior peroxidase-like activity of RuPtIrRhCu HEAzymes

RuPtIrRhCu HEAzymes could efficiently catalyze the oxidation of TMB both in the presence (Fig. 2a) and absence (Fig. S4a†) of hydrogen peroxide (H_2O_2), exhibiting POD- and OXD-like activity. However, compared with single metal NPs (Pt, Ir, Rh, Ru), the POD-like activity of HEAzymes was dramatically enhanced with the maximum initial reaction rate (Fig. 2b). The POD/OXD activity ratio is calculated to be (6.47) for HEAzymes, comparing with the ratio of Pt (1.56), Ir (4.02), Ru (7.80), Rh (3.00) (Fig. S4b†). The superior POD activity and large POD/OXD activity ratio are beneficial to reduce the interference of background signal and enhance the sensitivity in colorimetric detection. The enzymatic kinetics analysis shows that the K_m value of HEAzymes for TMB and H_2O_2 is calculated as 17.15 μM and 664.15 μM. The V_{max} of HEAzymes for TMB and H_2O_2 reaches 21.81×10^{-6} M s^{-1} and 18.3×10^{-6} M s^{-1}, respectively (Fig. 2d and e). As shown in Table S2,† the K_m values of RuPtIrRhCu HEAzymes toward substrates TMB and H_2O_2 are lower than those of HRP and many reported metal-based nanozymes, testifying a better affinity toward TMB and H_2O_2. It seems that the inherent coordination of five metal element introduced unique electronic structures and greatly improved the electron transfer efficiency. To evaluate the stability of HEAzymes, the POD-like activity of HEAzymes and single metal NPs were tested before and after storage at room temperature for six months. It could be observed in Fig. 2c that the POD-like activity of single metal NPs decreased to about 70% on average, while that of the HEAzymes was completely maintained without any decrease. The excellent stability of RuPtIrRhCu HEAzyme could be attributed to the high configurational entropy and severe lattice distortion, which make the HEAzyme more thermodynamically stable and reduce the possibility of phase separation, atomic migration, and microstructure change. Apparently, HEAzymes have greater application potential compared to single metal NPs. Moreover, HEAzymes exhibit evident time (Fig. 2a) and pH (Fig. 2f and S4c†) dependence. At 25 °C, the POD-like activity of HEAzymes is more than twice as that of single metal NPs. Particularly, HEAzymes seems to have better activity at temperature of 40–70 °C, when the activity of most natural enzymes may have been lost or inactivated (Fig. S4d†). Such characteristics endow HEAzymes with extensive application scenarios under both room temperature and some high-temperature conditions. ESR was utilized to detect intermediates in the catalytic process (Fig. S5†). When single metal NPs (Pt, Ir, Ru, Rh, Cu) or HEAzyme were added to the solution containing H_2O_2 and trapping agent (DMPO), no DMPO/$^{\bullet}$OH characteristic peaks were observed within 3 min of reaction. Only the solution added by Cu NPs produced a weak DMPO/$^{\bullet}$OH signal (Fig. S5a†). This result should be attributed to the strong $^{\bullet}$OH adsorption of noble metal and HEAzyme. Most of the $^{\bullet}$OH produced by the decomposition of H_2O_2 tends to absorb on the surface of nanozymes rather than exist in the solution in free

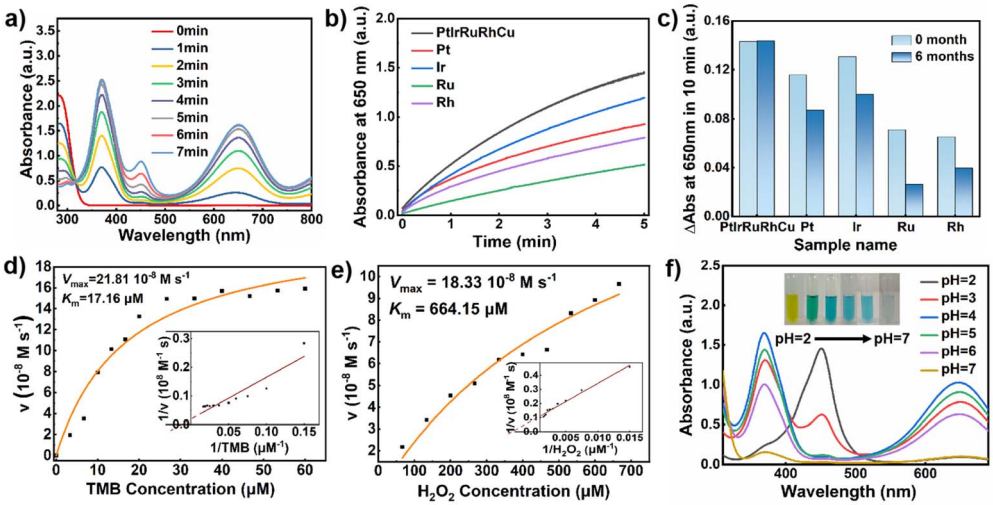

Fig. 2 POD-like activity of HEAzymes. (a) The UV-vis spectra of TMB in the presence of H_2O_2 catalyzed by HEAzymes with increasing time. (b) Comparison of POD-like activity of HEAzymes and single metal NPs (Pt, Ir, Ru, Rh) at 25 °C. (c) Comparison of POD-like catalytic stability of HEAzymes and single metal NPs before and after storage of 6 months. (d and e) Michaelis–Menten curves of the HEAzymes with different concentrations of H_2O_2 and TMB. (f) POD-like activity of HEAzymes under different pH conditions.

state. The weak DMPO/˙OH signal seems to come from the Fenton-like reaction introduced by Cu^{2+} ions on the Cu NPs. To verify the above discussion, Fe^{2+} was added to the catalytic system for promoting the production of ˙OH in the blank group. Upon the addition of single metal NPs (except for Cu) and HEAzyme, distinct lower signal intensities were detected, which is consistent with the phenomenon reported in previous studies[39,40] and further confirmed the adsorption of ˙OH on the surface of nanozymes.

Mechanism for enhanced POD-like activity of RuPtIrRhCu HEAzymes

First-principles calculations were employed to elucidate the enhanced POD-like activity of the alloy compared to pure metals Ru, Pt, Ir, Rh, and Cu. The details of the material structures defined during the calculations were presented in Table S1.† Building upon our previous investigations,[41,42] the mechanism underlying the POD-mimicking activity on metal/alloy surfaces primarily involves two processes: initially, the activation of H_2O_2 to generate highly reactive radicals such as *OH or O* (where * denotes the adsorbed state) on the surface, followed by hydrogen abstraction from substrates like TMB. Consequently, we proposed a mechanism, as shown in Fig. 3a, and computed the energy profiles for various metal/alloy surfaces. The results (detailed in Fig. 3b) show that except for Ru, where H_2O_2 dissociates directly into two *OH radicals, all $H_2O_2^*$ intermediates were located on single metal NPs. Following this, the O–O bond in $H_2O_2^*$ cleaves, generating two *OH radicals and releasing energy (step 1 to step 3). For single metals NPs excluding Pt, hydrogen transfer likely occurs between the two *OH radicals to form H_2O and O*, a step characterized by either negative or marginally positive reaction energies, except on Pt where it is notably high as 0.76 eV (step 4). The generated O* can capture reductive hydrogen from the substrate TMB in two sequential steps, first forming *OH and then H_2O* and thus freeing the active site (step 5). Obviously, for the *OH absorbed on Pt, direct hydrogen transfer between two *OH is unfeasible. They tend to independently capture reducing hydrogen from TMB, overcoming a low energy barrier of 0.26 eV. This hydrogen capture reaction, whether it is the first or second step, constitutes the rate-determining step (RDS) in catalysis for these surfaces, accompanied by an increase in energy. Furthermore, the potential energy surface for Ru is significantly lower compared to other metals, with strong adsorption of reactive oxygen intermediates leading to the active site being saturated with *OH and O* (Step 4). If the abundant *OH or O* is unable to be transferred effectively, blocking will occur, resulting in a high oxidative desorption energy barrier (1.86 eV in step 5) and serious reduction of POD activity, which is consistent with the results shown in Fig. 2b.

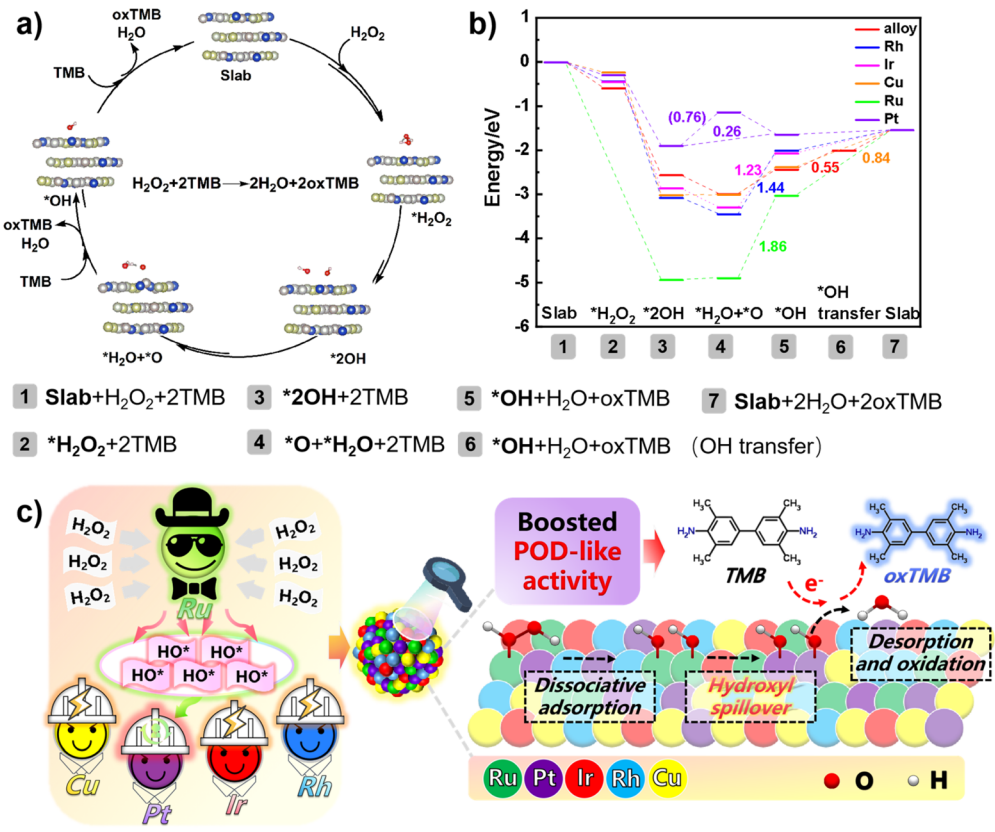

Fig. 3 (a) Proposed mechanism for the POD-like activity of the pure metals of Rh, Ir, Cu, Ru, and Pt as well as HEA alloy. The (111) surface of alloy was used as the structural model for illustration. (b) Energy profile corresponding to the proposed mechanism on different metals and HEA alloy, containing the chemical species composition for each energy minima in panel (b). (c) Schematic diagram for hydroxyl spillover mechanism in POD-like catalysis of RuPtIrRhCu HEAzymes.

In RuPtIrRhCu HEA alloy, the preferred adsorption site was also determined as Ru atom, where the dissociative adsorption of $H_2O_2^*$ has the lowest thermodynamic energy. However, the generated *OH can migrate across the surface, rather than being congested and restricted on Ru atom. When *OH reaches the top of the Pt atom, which has a low adsorption capacity, it is easily desorbed, completing the catalytic cycle with a modest energy increase of 0.55 eV (step 6). The sequential energy increases for the RDS are as follows: Pt (0.26 eV) < alloy (0.55 eV) < Cu (0.84 eV) < Ir (1.23 eV) < Rh (1.44 eV) < Ru (1.86 eV). Therefore, the "hydroxyl spillover" from Ru to Pt in the alloy brings a better catalytic route (lower energy barrier) compared to the single metal site (Cu, Ir, Rh, and Ru). Furthermore, the alloy displayed the most negative adsorption energy ($E_{ads,\ H_2O_2}$), indicating the strongest interaction with H_2O_2. Compared to Pt, the stronger adsorption of H_2O_2 on the alloy is crucial in facilitating the excitation of more H_2O_2 molecules. Thus, the designed RuPtIrRhCu HEAzymes exhibit significantly enhanced catalytic performance in experimental tests. Learning from the "volcano model",[43,44] where the adsorption energy of *OH ($E_{ads,\ OH}$) serves as the descriptor for POD-like activity, the "hydroxyl spillover" mechanism seems to adequately liberate the functions of different elements, achieving the multi-site collaborating effect to introduce better catalytic efficiency (as schematically depicted in Fig. 3c).

It should be particularly pointed out that, although the preferred *OH migration path (Ru to Pt) is proposed, considering the complexity of the catalytic interface of HEAzymes, the role of the remaining elements (Ir, Rh and Cu) should not be ignored. The d-band theory,[45] initially developed for metallic systems, distinctly clarifies the root cause of the high catalytic activity observed in alloy. A higher d-band center correlates with stronger adsorption energies for *OH.[13] The gradient d-band centers introduced by Ir, Rh, and Cu promote multi-site orbital coupling among Ru, Pt, Ir, Rh, and Cu is activated, which in turn subtly tunes the electronic structure of the alloy. This tuning provides the alloy a suitable reaction micro-environments for O–O bond activation and *OH desorption, with the d-band center of 1.85 eV (Fig. S6†). In this scenario, the d-band center of Ru exhibits the highest value at −1.23 eV, while Pt displays the lowest height at −2.40 eV, aligning well with the proposed "hydroxyl spillover" path from Ru to Pt (Fig. S6†). Furthermore, the other three elements (Ir, Rh and Cu) may also serve as the intermediate sites in *OH migration or *OH desorption. We will continue exploring the possible hydroxyl spillover paths in subsequent studies, expecting to deeply reveal the mechanism for superior catalytic activity of HEAzymes.

Multi-channel colorimetric sensing platform based on RuPtIrRhCu HEAzymes

A multi-channel colorimetric sensing platform was constructed based on the boosted POD-like activity of RuPtIrRhCu HEAzymes. It is proven that the solution's color is mainly derived from the blue charge transfer complex, which is composed of diamine (TMB) and diimine (TMB^{2+}). The corresponding UV-vis absorption peaks are located at 370 nm and 650 nm, respectively. Moreover, TMB^{2+} with a yellow absorption peak at 450 nm could be motivated in an acidic solution. At a pH of less than 2, the solution will turn yellow and only one absorption peak at 450 nm could be observed. Therefore, it is not suitable for colorimetric sensing arrays due to the lack of adequate sensing elements. At pH = 3, the solution is green, with three distinct absorption peaks clearly visible at 450 nm. As the pH level of the solution increases, the solution absorbance at 450 nm gradually decreases, and its color changed from green to blue until eventual color disappearance at pH = 7 (Fig. 2f). By integrating absorption peaks (370 nm, 450 nm, and 650 nm) stimulated by HEAzymes in pH = 3 buffer solution, a multi-channel colorimetric sensor array was designed and applied in detecting biological antioxidants.

This HEAzymes-based sensing platform was applied in detecting biological antioxidants. After adding different biological antioxidants (L-Cys, D-Cys, GSH, NaSH, NAC, TA, GA, and DA), TMB oxidation by HEAzymes caused a varying degree of reduction at 370 nm (ΔA_{370}), 450 nm (ΔA_{450}), and 650 nm (ΔA_{650}). This cross-reactive property is convenient for us to analyze the absorbance alterations at 370 nm (ΔA_{370}), 450 nm (ΔA_{450}) and 650 nm (ΔA_{650}). By taking color measurements of ΔA_{370}, ΔA_{450}, and ΔA_{650}, fingerprints were created to identify different biological antioxidants (Fig. 4). The superiority of HEAzymes in identifying biological antioxidants was highlighted by comparing the detection capabilities of HRP and Pt NPs (Fig. 4a). The oxidation catalyzed by HRP was obviously diminished in pH = 3 buffer solution *versus* aqueous solution, which is an inherent trait of natural enzymes. Compared to Pt NPs, HEAzymes exhibited significantly stronger catalysis capacity in TMB oxidation, with stronger intensity for the three absorption peaks. As shown in Fig. 4b and c, pH = 3 buffer solution (2.7 mL) containing only TMB (20 mM, 20 μL), H_2O_2 (0.1 M, 20 μL) was set as the blank control. Adding NaSH, L-Cys, TA, D-Cys, GSH, NAC, GA and DA at 0.2 mM concentration was seen to induce significant absorption intensity differences at 370 nm, 450 nm, and 650 nm. The internal mechanism may be elaborated as different functional groups (such as amino and sulfydryl groups) enable the absorption of bio-antioxidants to the surface of HEAzymes. The interactions between bio-antioxidants and HEAzymes affect the affinity between substrate and active sites, finally weakening the catalytic activity of HEAzymes to a different extent. Principal component analysis (PCA) revealed the apparent clustering of points into eight distinct groups, corresponding to the eight different antioxidants, demonstrating excellent discriminating ability. The platform potential in distinguishing target analytes with similar functional groups and molecular weight (*e.g.* chiral molecules) was further explored by detecting L-Cys, D-Cys, and their mixtures with varying ratios at 13 μM total concentration, and the five test groups showed significant differences (Fig. 4e). PCA results showed effective clustering of L-Cys, D-Cys and their mixtures at three ratios into five separate groups, confirming chiral cysteins could be accurately distinguished (Fig. 4f), and demonstrating the establishment of an accurate and efficient L-Cys detection method (Fig. 4g–i). Specifically, with increasing concentration, the intensity of the three characteristic absorption peaks gradually diminished, accompanied with lightening of solution color (Fig. 4g). A good relationship can be observed

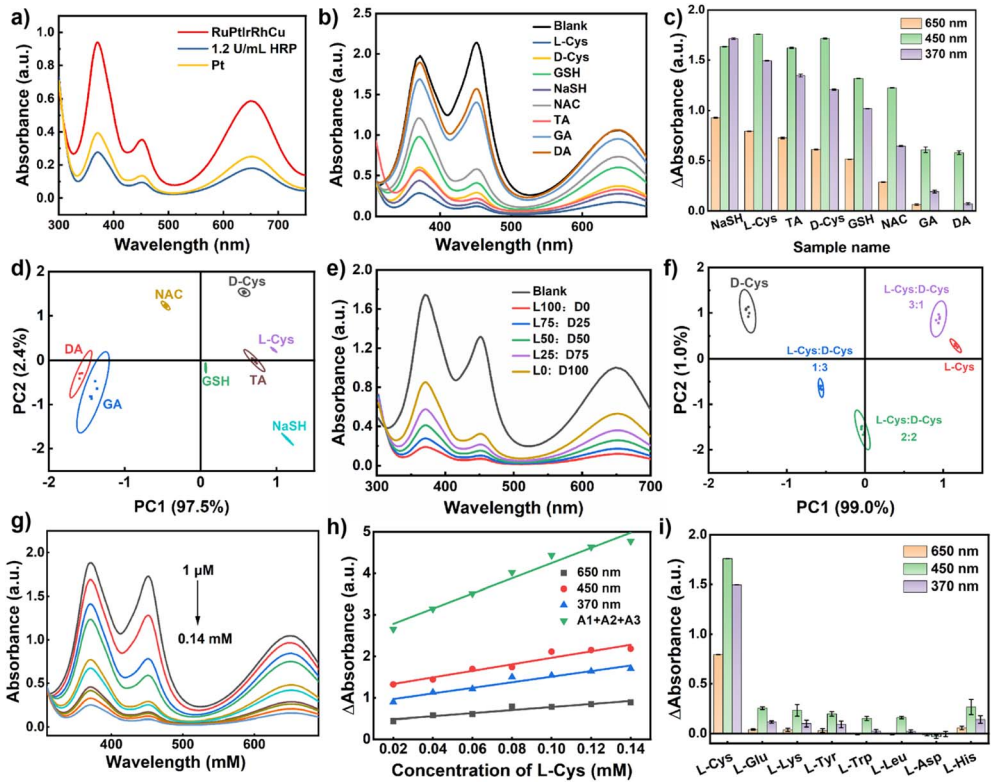

Fig. 4 Multi-channel colorimetric sensing platform based on RuPtIrRhCu HEAzymes: (a) TMB oxidation catalyzed by RuPtIrRhCu, Pt and HRP in different solutions after 10 min reaction (pH = 3 buffer). (b) UV-vis spectra and (c) colorimetric response patterns before and after adding eight kinds of antioxidants (NaSH, L-Cys, TA, D-Cys, GSH, NAC, GA and DA) with 0.2 mM concentration. (d) PCA score plot for discrimination of eight antioxidant tested five times. (e) UV-vis spectra and (f) PCA score plot for discriminating mixtures of L-Cys and D-Cys at different ratios (total pesticides concentration 13 μM) tested five times. (g) UV-vis spectra of HEAzymes in the absence and presence of different concentrations of L-Cys (200 μL 1, 5, 10, 20, 40, 60, 80, 100, 120, 140 μM). (h) Linear fitting curves of absorbance attenuation at 370 nm ($A_{370\ nm}$), 450 nm ($A_{450\ nm}$), 650 nm ($A_{650\ nm}$) and total change ($A_{370\ nm} + A_{450\ nm} + A_{650\ nm}$) for determination of L-Cys. The error bars show the standard deviation of five tests. (i) Colorimetric response patterns of 200 μL L-Cys (100 μM) towards the 200 μL 40-fold concentration (4 mM) of multifarious amino acid interferents (L-GLu, L-Lys, L-Tyr, L-Trp, L-Leu, L-Asp, and L-His).

in the concentration range of 0.02 mM to 0.2 mM in the four calibration curves ($A_{370\ nm}$,, $A_{450\ nm}$, $A_{650\ nm}$, and $A_{650\ nm} + A_{450\ nm} + A_{370\ nm}$, simplified as $A_1 + A_2 + A_3$), with a correlation coefficient (R^2) of 0.95, as well as theoretical sensitivities of 6.75 ($A_{370\ nm}$), 7.89 ($A_{450\ nm}$), 3.67 ($A_{650\ nm}$), and 18.30 ($A_1 + A_2 + A_3$) mM^{-1}, respectively (Fig. 4h). Additionally, the sensor array exhibited the limit of detection (LOD) of 0.15 μg mL^{-1} (0.0012 mM, S/N = 3), with excellent specificity for L-Cys (100 μM) to the 40-fold concentration (4 mM) of multifarious amino acid interferents (L-GLu, L-Lys, L-Tyr, L-Trp, L-Leu, L-Asp, L-His) at 200 μL solution volume (Fig. 4i). Furthermore, the standard addition method was employed to assess the NAC content in a clinical complex amino acid injection (Table S3†), achieving optimal recoveries from 99.46 to 117.10%.

Conclusions

In summary, we successfully fabricated a novel RuPtIrRhCu HEAzyme by multi-element matching design. Experimental and theoretical studies demonstrate remarkable *OH absorption affinity and infusive hydroxyl spillover effect for RuPtIrRhCu HEAzymes, which contribute to ultra-boosted POD-like activity. Additionally, we developed a HEAzymes-based sensing platform containing a multi-channel sensor array providing three response pattern recognition ($A_{650nm} + A_{450nm} + A_{370nm}$). Eight kinds of biological antioxidants (NaSH, L-Cys, D-Cys, NAC, GSH, DA, GA, TA) were successfully identified. Highly accurate and effective detection for L-Cys was achieved, with a LOD of 0.15 μg mL^{-1}. This work provides a novel strategy for rational design of HEAzymes and facilitates the understanding in multi-element collaboration mechanism of catalytic activity, which may inspire extensive and deep explorations for engineering high-performance nanozyme. Furthermore, although the HEAzyme-based sensor has certain potential in synergistically improving the catalytic activity, selectivity, and stability. Bottlenecks in batch synthesis and signal separation under complex substrates or external environments still limits its industrial application. In the future, material rational design, technology integration and standardization construction of HEAzymes deserve more attention.

Data availability

The data supporting this article have been included as part of the ESI.†

Author contributions

The manuscript was written through contributions of all authors. All authors have given approval to the final version of the manuscript. Qi Yang: conceptualization, data curation, formal analysis, funding acquisition, investigation, methodology, visuaization, writing – original draft. Jiawei Zhang: data curation, formal analysis, visuaization, writing – original draft. Yuxi Tang: data curation, visuaization. Yan Ju: data curation. Xuejiao Gao: conceptualization, formal analysis, funding acquisition, visuaization, software, writing – review & editing. Chaoyang Chu: investigation, resources. Huimin Jia: conceptualization, funding acquisition, visuaization, writing – review & editing. Weiwei He: conceptualization, resources, validation, visuaization, writing – review & editing.

Conflicts of interest

The authors declare that they have no known competing financial interests or personal relationships that could have appeared to influence the work reported in this paper.

Acknowledgements

This work is supported financially by the National Natural Science Foundation of China (62274141, 22467013), the Henan Provincial Science and Technology Research Project (242102230074), the Gan Poyang talents support program, academic and technical leaders of major disciplines (20232BCJ23014). We thank Dr Shitao Wu from ShanghaiTech University for his assistance of HRTEM analysis.

References

1 C. Liu, M. Zhang, H. Q. Geng, P. Zhang, Z. Zheng, Y. L. Zhou and W. W. He, NIR enhanced peroxidase-like activity of Au@CeO_2 hybrid nanozyme by plasmon-induced hot electrons and photothermal effect for bacteria killing, *Appl. Catal., B*, 2021, **295**, 120317.

2 J. W. Gong, Q. Liu, L. L. Cai, Q. Yang, Y. P. Tong, X. Chen, K. Sumasri, X. B. Mao and W. W. He, Multimechanism collaborative superior antioxidant CDzymes to alleviate salt stress-induced oxidative damage in plant growth, *ACS Sustain. Chem. Eng.*, 2023, **11**(10), 4237–4247.

3 J. Zhao, J. W. Gong, J. N. Wei, Q. Yang, G. J. Li, Y. P. Tong and W. W. He, Metal organic framework loaded fluorescent nitrogen-doped carbon nanozyme with light regulating redox ability for detection of ferric ion and glutathione, *J. Colloid Interface Sci.*, 2022, **618**, 11–21.

4 Y. Y. Mao, F. M. Jia, T. Y. Jing, T. T. Li, H. M. Jia and W. W. He, Enhanced multiple enzymelike activity of PtPdCu trimetallic nanostructures for detection of Fe^{2+} and evaluation of antioxidant capabilit, *ACS Sustain. Chem. Eng.*, 2021, **9**(1), 569–579.

5 Y. X. Li, L. L. Yang, Y. J. Liao, R. Z. Zhao, L. Z. Ji, R. Su, D. K. Xu and F. H. Wang, Photothermal Heating-Assisted Superior Antibacterial and Antibiofilm Activity of High-Entropy-Alloy Nanoparticles, *Adv. Funct. Mater.*, 2023, **33**(35), 2302712.

6 X. X. Zhu, H. Y. Li, S. T. Hou, P. Song, J. L. Zheng, T. Wu, H. Zhao and Q. Y. Liu, A novel three-stage continuous sensing platform for H_2O_2 and cholesterol based on $CuFeS_2$ nanozyme: Theoretical calculation and experimental verification, *Chem. Eng. J.*, 2024, **482**, 148589.

7 X. X. Zhu, H. Y. Li, T. Wu, K. L. Wu, W. J. Xu, F. J. Qin, W. X. Chen, J. L. Zheng and Q. Y. Liu, In situ decorating the surface and interlayer of montmorillonite with $Co_{0.5}Ni_{0.5}Fe_2O_4$ nanoparticles: A sustainable, biocompatible colorimetric platform for H_2O_2 and acetylcholine, *Nano Res.*, 2022, **15**(10), 9319–9326.

8 X. X. Zhu, Y. Xue, S. T. Hong, P. Song, T. Wu, H. Zhao, N. A. Osman, A. K. Alanazi, Y. Gao, H. M. Abo-Dief, H. D. Li, B. B. Xu, P. Wasnik and Q. Y. Liu, Highly selective colorimetric platinum nanoparticle-modified core-shell molybdenum disulfide/silica platform for selectively detecting hydroquinone, *Adv. Compos. Hybrid Mater.*, 2023, **6**, 142.

9 L. Z. Gao, J. Zhuang, L. Nie, J. B. Zhang, Y. Zhang, N. Gu, T. H. Wang, J. Feng, D. L. Yang, S. Perrett and X. Y. Yan, Intrinsic peroxidase-like activity of ferromagnetic nanoparticles, *Nat. Nanotechnol.*, 2007, **2**(9), 577–583.

10 H. Wei and E. Wang, Nanomaterials with enzyme-like characteristics (nanozymes): next-generation artificial enzymes, *Chem. Soc. Rev.*, 2013, **42**(14), 6060–6093.

11 Q. Q. Wang, H. Wei, Z. Q. Zhang, E. Wang and S. J. Dong, Nanozyme: An emerging alternative to natural enzyme for biosensing and immunoassay, *TrAC, Trends Anal. Chem.*, 2018, **105**, 218–224.

12 H. Wang, K. W. Wan and X. H. Shi, Recent Advances in Nanozyme Research, *Adv. Mater.*, 2019, **31**(45), 1805368.

13 Z. Xi, K. C. Wei, Q. X. Wang, M. J. Kim, S. H. Sun, V. Fung and X. H. Xia, Nickel-Platinum Nanoparticles as Peroxidase Mimics with a Record High Catalytic Efficiency, *J. Am. Chem. Soc.*, 2021, **143**(7), 2660–2664.

14 S. F. Ji, B. Jiang, H. Hao, Y. J. Chen, J. C. Dong, Y. Mao, Z. D. Zhang, R. Gao, W. X. Chen, R. F. Zhang, Q. Liang, H. J. Li, S. H. Liu, Y. Wang, Q. H. Zhang, L. Gu, D. Duan, M. Liang, D. S. Wang, X. Y. Yan and Y. D. Li, Matching the kinetics of natural enzymes with a single-atom iron nanozyme, *Nat. Catal.*, 2021, **4**(5), 407–417.

15 X. P. Zhi, Q. Yang, X. H. Zhang, H. B. Zhang, Y. Gao, L. L. Zhang, Y. P. Tong and W. W. He, Copper regulation of PtRhRuCu nanozyme targeted boosting peroxidase-like activity for ultrasensitive smartphone-assisted colorimetric sensing of glucose, *Food Chem.*, 2024, **445**, 138788.

16 J. J. Zheng, Z. Z. Wang and X. F. Gao, Nonradical Surface Chemistry Mechanisms for Catalytic Nanoparticles, *J. Phys. Chem. Lett.*, 2024, **15**(7), 1887–1889.

17 X. J. Gao, Y. L. Zhao and X. F. Gao, Catalytic Signal Transduction Theory Enabled Virtual Screening of Nanomaterials for Medical Functions, *Acc. Chem. Res.*, 2023, **56**(17), 2366–2377.

18 X. J. Gao, K. Ciura, Y. J. Ma, A. Mikolajczyk, K. Jagiello, Y. X. Wan, Y. R. Gao, J. J. Zheng, S. L. Zhong, T. Puzyn and

X. F. Gao, Toward the Integration of Machine Learning and Molecular Modeling for Designing Drug Delivery Nanocarriers, *Adv. Mater.*, 2024, **36**(45), 2407793.

19 X. M. Shen, Z. Z. Wang, X. J. Gao and X. F. Gao, Reaction Mechanisms and Kinetics of Nanozymes: Insights from Theory and Computation, *Adv. Mater.*, 2024, **36**(10), 2211151.

20 Z. W. Chen, J. Li, P. Ou, J. E. Huang, Z. Wen, L. Chen, X. Yao, G. Cai, C. C. Yang, C. V. Singh and Q. Jiang, Unusual Sabatier principle on high-entropy alloy catalysts for hydrogen evolution reactions, *Nat. Commun.*, 2024, **15**, 359.

21 J. Li, J. Hu, M. Zhang, W. Gou, S. Zhang, Z. Chen, Y. Qu and Y. Ma, A fundamental viewpoint on the hydrogen spillover phenomenon of electrocatalytic hydrogen evolution, *Nat. Commun.*, 2021, **12**, 3502.

22 H. Q. Fu, M. Zhou, P. F. Liu, P. Liu, H. Yin, K. Z. Sun, H. G. Yang, M. Al-Mamun, P. Hu, H. F. Wang and H. Zhao, Hydrogen Spillover-Bridged Volmer/Tafel Processes Enabling Ampere-Level Current Density Alkaline Hydrogen Evolution Reaction under Low Overpotential, *J. Am. Chem. Soc.*, 2022, **144**(13), 6028–6039.

23 Y. Shen, X. L. Zhang, M. R. Qu, J. Ma, S. Zhu, Y. L. Min, M. R. Gao and S. H. Yu, Cr dopant mediates hydroxyl spillover on RuO_2 for high-efficiency proton exchange membrane electrolysis, *Nat. Commun.*, 2024, **15**, 7861.

24 Z. T. Yan, S. Tao, J. Wang, X. L. Lu and T. B. Lu, Unlocking Efficient Alkaline Hydrogen Evolution Through Ru–Sn Dual Metal Sites and a Novel Hydroxyl Spillover Effect, *Adv. Mater.*, 2024, **36**(46), 2411942.

25 C. Liu, Y. Y. Yan, X. W. Zhang, Y. Y. Mao, X. Q. Ren, C. Y. Hu, W. W. He and J. J. Yin, Regulating the pro- and anti-oxidant capabilities of bimetallic nanozymes for the detection of Fe^{2+} and protection of Monascus pigments, *Nanoscale*, 2020, **12**(5), 3068–3075.

26 T. A. A. Batchelor, T. Löffler and B. Xiao, Complex-Solid-Solution Electrocatalyst Discovery by Computational Prediction and High-Throughput Experimentation, *Angew. Chem., Int. Ed.*, 2021, **60**(13), 6932–6937.

27 K. Y. Tsai, M. H. Tsai and J. W. Yeh, Sluggish diffusion in Co–Cr–Fe–Mn–Ni high-entropy alloys, *Acta Mater.*, 2013, **61**(13), 4887–4897.

28 D. S. Wu, K. Kusada, T. Yamamoto, T. Toriyama, S. Matsumura, I. Gueye, O. Seo, J. Kim, S. Hiroi, O. Sakata, S. Kawaguchi, Y. Kubota and H. Kitagawa, On the electronic structure and hydrogen evolution reaction activity of platinum group metal-based high-entropy-alloy nanoparticles, *Chem. Sci.*, 2020, **11**(47), 12731–12736.

29 P. Malinovskis, S. Fritze, L. Riekehr, L. von Fieandt, J. Cedervall, D. Rehnlund, L. Nyholm, E. Lewin and U. Jansson, Synthesis and characterization of multicomponent (CrNbTaTiW)C films for increased hardness and corrosion resistance, *Mater. Des.*, 2018, **149**, 51–62.

30 E. P. George, D. Raabe and R. O. Ritchie, High-entropy alloys, *Nat. Rev. Mater.*, 2019, **4**(8), 515–534.

31 Y. Zhang, T. T. Zuo and Z. Tang, Microstructures and properties of high-entropy alloys, *Prog. Mater. Sci.*, 2014, **61**, 1–93.

32 K. Kong, J. Hyun and Y. Kim, Nanoporous structure synthesized by selective phase dissolution of AlCoCrFeNi high-entropy alloy and its electrochemical properties as supercapacitor electrode, *J. Power Sources*, 2019, **437**, 226927.

33 Y. Ai, M. Q. He, H. Sun, X. Jia, L. Wu, X. Zhang, H. B. Sun and Q. Liang, Ultra-Small High-Entropy Alloy Nanoparticles: Efficient Nanozyme for Enhancing Tumor Photothermal Therapy, *Adv. Mater.*, 2023, **35**(23), 2302335.

34 H. Li, J. Lai and Z. Li, Multi-Sites Electrocatalysis in High-Entropy Alloys, *Adv. Funct. Mater.*, 2021, **31**(47), 2106715.

35 X. Han, G. Wu, S. Zhao, J. Guo, M. Yan, X. Hong and D. Wang, Nanoscale high-entropy alloy for electrocatalysis, *Matter*, 2023, **6**(6), 1717–1751.

36 M. Luo and S. Guo, Strain-controlled electrocatalysis on multimetallic nanomaterials, *Nat. Rev. Mater.*, 2017, **2**, 17059.

37 X. Huang, G. Yang and S. Li, Noble-metal-based high-entropy-alloy nanoparticles for electrocatalysis, *J. Energy Chem.*, 2022, **68**, 721–751.

38 J. T. Ren, L. Chen, H. Y. Wang and Z. Y. Yuan, High-entropy alloys in electrocatalysis: from fundamentals to applications, *Chem. Soc. Rev.*, 2023, **52**(23), 8319–8373.

39 Y. J. Tang, Y. J. Chen, Y. Wu, W. Q. Xu, Z. Luo, H. R. Ye, W. L. Gu, W. Y. Song, S. J. Guo and C. Z. Zhu, High-Indexed Intermetallic Pt3Sn Nanozymes with High Activity andSpecificity for Sensitive Immunoassay, *Nano Lett.*, 2023, **23**(1), 267–275.

40 M. D. Lei, X. L. Ding, J. Liu, Y. J. Tang, H. X. Chen, Y. Zhou, C. Z. Zhu and H. Y. Yan, Trace Amount of Bi-Doped Core–Shell Pd@Pt Mesoporous Nanospheres with Specifically Enhanced Peroxidase-Like Activity Enable Sensitive and Accurate Detection of Acetylcholinesterase and Organophosphorus Nerve Agents, *Anal. Chem.*, 2024, **96**(15), 6072–6078.

41 X. M. Shen, Z. Z. Wang, X. J. Gao and X. F. Gao, Reaction Mechanisms and Kinetics of Nanozymes: Insights from Theory and Computation, *Adv. Mater.*, 2023, **36**(10), 2211151.

42 X. M. Shen, W. Q. Liu, X. J. Gao, Z. H. Lu, X. C. Wu and X. F. Gao, Mechanisms of Oxidase and Superoxide Dismutation-like Activities of Gold, Silver, Platinum, and Palladium, and Their Alloys: A General Way to the Activation of Molecular Oxygen, *J. Am. Chem. Soc.*, 2015, **137**(50), 15882–15891.

43 X. M. Shen, Z. Z. Wang, X. F. Gao and Y. L. Zhao, Density Functional Theory-Based Method to Predict the Activities of Nanomaterials as Peroxidase Mimics, *ACS Catal.*, 2020, **10**(21), 12657–12665.

44 Activity and Selectivity Maps, in *Fundamental Concepts in Heterogeneous Catalysis*, 2014, pp 97–113.

45 B. Hammer and J. K. Norskov, Why gold is the noblest of all the metals, *Nature*, 1995, **376**(6537), 238–240.